LETTER

https://doi.org/10.1038/s41586-018-0060-z

The pressure distribution inside the proton

V. D. Burkert[1]*, L. Elouadrhiri[1] & F. X. Girod[1]

The proton, one of the components of atomic nuclei, is composed of fundamental particles called quarks and gluons. Gluons are the carriers of the force that binds quarks together, and free quarks are never found in isolation—that is, they are confined within the composite particles in which they reside. The origin of quark confinement is one of the most important questions in modern particle and nuclear physics because confinement is at the core of what makes the proton a stable particle and thus provides stability to the Universe. The internal quark structure of the proton is revealed by deeply virtual Compton scattering[1,2], a process in which electrons are scattered off quarks inside the protons, which subsequently emit high-energy photons, which are detected in coincidence with the scattered electrons and recoil protons. Here we report a measurement of the pressure distribution experienced by the quarks in the proton. We find a strong repulsive pressure near the centre of the proton (up to 0.6 femtometres) and a binding pressure at greater distances. The average peak pressure near the centre is about 10^{35} pascals, which exceeds the pressure estimated for the most densely packed known objects in the Universe, neutron stars[3]. This work opens up a new area of research on the fundamental gravitational properties of protons, neutrons and nuclei, which can provide access to their physical radii, the internal shear forces acting on the quarks and their pressure distributions.

The basic mechanical properties of the proton are encoded in the gravitational form factors (GFFs) of the energy–momentum tensor[1,4,5]. Graviton–proton scattering is the only known process that can be used to directly measure these form factors[4,6], whereas generalized parton distributions[2,7,8] enable indirect access to the basic mechanical properties of the proton[2].

A direct determination of the quark pressure distribution in the proton (Fig. 1) requires measurements of the proton matrix element of the energy–momentum tensor[9]. This matrix element contains three scalar GFFs that depend on the four-momentum transfer t to the proton. One of these GFFs, $d_1(t)$, encodes the shear forces and pressure distribution on the quarks in the proton, and the other two, $M_2(t)$ and $J(t)$, encode the mass and angular momentum distributions. Experimental information on these form factors is essential to gain insight into the dynamics of the fundamental constituents of the proton. The framework of generalized parton distributions (GPDs)[2,7,8] has provided a way to obtain information on $d_1(t)$ from experiments. The most effective way to access GPDs experimentally is deeply virtual Compton scattering (DVCS)[1,2], where high-energy electrons (e) are scattered from the protons (p) in liquid hydrogen as $e\,p \rightarrow e'\,p'\,\gamma$, and the scattered electron (e'), proton (p') and photon (γ) are detected in coincidence. In this process, the quark structure is probed with high-energy virtual photons that are exchanged between the scattered electron and the proton, and the emitted (real) photon controls the momentum transfer t to the proton, while leaving the proton intact. Recently, methods have been developed to extract information about the GPDs and the related Compton form factors (CFFs) from DVCS data[10–13].

To determine the pressure distribution in the proton from the experimental data, we follow the steps that we briefly describe here. We note that the GPDs, CFFs and GFFs apply only to quarks, not to gluons.
(1) We begin with the sum rules that relate the Mellin moments of the GPDs to the GFFs[1].
(2) We then define the complex CFF, $\mathcal{H}$, which is directly related to the experimental observables describing the DVCS process, that is, the differential cross-section and the beam-spin asymmetry.
(3) The real and imaginary parts of $\mathcal{H}$ can be related through a dispersion relation[14–16] at fixed t, where the term $D(t)$, or D-term, appears as a subtraction term[17].
(4) We derive $d_1(t)$ from the expansion of $D(t)$ in the Gegenbauer polynomials of ξ, the momentum transfer to the struck quark.
(5) We apply fits to the data and extract $D(t)$ and $d_1(t)$.
(6) Then, we determine the pressure distribution from the relation between $d_1(t)$ and the pressure $p(r)$, where r is the radial distance from the proton's centre, through the Bessel integral.

The sum rules that relate the second Mellin moments of the chiral-even GPDs to the GFFs are[1]:

$$\int x\,[H(x,\xi,t)+E(x,\xi,t)]\,\mathrm{d}x = 2J(t)$$

$$\int xH(x,\xi,t)\mathrm{d}x = M_2(t)+\frac{4}{5}\xi^2 d_1(t)$$

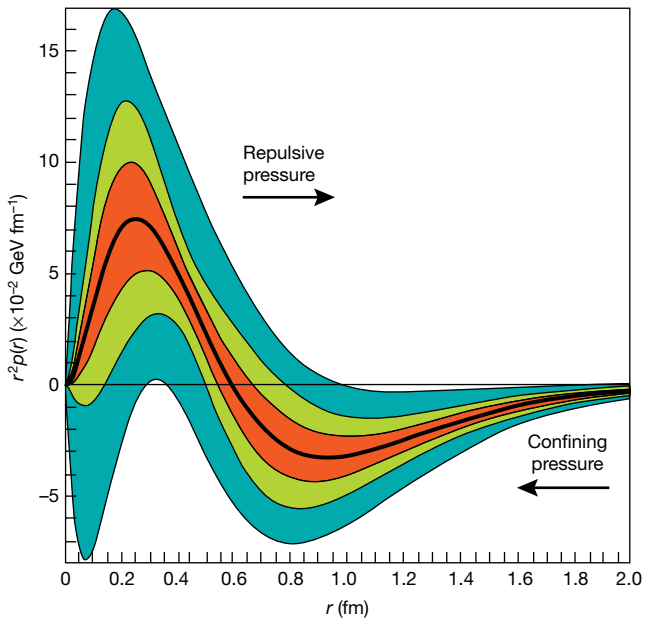

Fig. 1 | Radial pressure distribution in the proton. The graph shows the pressure distribution $r^2p(r)$ that results from the interactions of the quarks in the proton versus the radial distance r from the centre of the proton. The thick black line corresponds to the pressure extracted from the D-term parameters fitted to published data[22] measured at 6 GeV. The corresponding estimated uncertainties are displayed as the light-green shaded area shown. The blue area represents the uncertainties from all the data that were available before the 6-GeV experiment, and the red shaded area shows projected results from future experiments at 12 GeV that will be performed with the upgraded experimental apparatus[30]. Uncertainties represent one standard deviation.

[1]Thomas Jefferson National Accelerator Facility, Newport News, VA, USA. *e-mail: burkert@jlab.org

where H and E are the GPDs corresponding to the nucleon helicity-conserving and helicity-flip processes, respectively; x and ξ are the average and the transferred quark momentum fractions, respectively; and $M_2(t)$, $J(t)$ and $d_1(t)$ correspond to the time–time, time–space and space–space components of the energy–momentum tensor, respectively. We have some constraints on $M_2(t)$ and $J(t)$ from theory and previous work; namely, at $t=0$ they are fixed to the proton's mass and spin, respectively. By contrast, almost nothing is known about the equally fundamental quantity $d_1(t)$. As the GFF $d_1(t)$ encodes the shear forces on the quarks and the pressure distribution in the proton, we can expect the existence of a zero-sum rule ensuring that the total pressure and forces vanish, thus preserving the stability of the dynamics. The observables are parameterized by the CFFs, which for the GPD H are the real quantities $\mathrm{Re}\mathcal{H}$ and $\mathrm{Im}\mathcal{H}$ defined by:

$$\mathrm{Re}\mathcal{H}(\xi,t)+i\mathrm{Im}\mathcal{H}(\xi,t)=\int_{-1}^{1}\mathrm{d}x\left(\frac{1}{\xi-x-\mathrm{i}\epsilon}-\frac{1}{\xi+x-\mathrm{i}\epsilon}\right)H(x,\xi,t) \quad (1)$$

The average quark momentum fraction x is not observable in this process; it is integrated over with the inverse of the quark momentum fractions shifted from the real axis by an infinitesimal positive number ϵ. The analytical properties of the amplitude $\mathcal{H}$ (as a complex function) in the leading-order approximation lead to the dispersion relation:

$$\mathrm{Re}\mathcal{H}(\xi,t)\overset{\mathrm{lo}}{=}D(t)+\mathcal{P}\int_{-1}^{1}\mathrm{d}x\left(\frac{1}{\xi-x}-\frac{1}{\xi+x}\right)\mathrm{Im}\mathcal{H}(x,t)$$

where $\mathcal{P}$ is the principal part of the integral and the subtraction constant is the D-term. This approach allows us to replace one unknown complex CFF in the dispersion relation with its imaginary part and the D-term[18,19].

We derive $d_1(t)$ as the first coefficient in the Gegenbauer expansion of the D-term. Here, we truncate this expansion to $d_1(t)$ only.

$$D(t)=\frac{1}{2}\int_{-1}^{1}\frac{D(z,t)}{1-z}\mathrm{d}z$$

with

$$D(z,t)=(1-z^2)\,[d_1(t)C_1^{3/2}(z)+\cdots]$$

and

$$-1<z=\frac{x}{\xi}<1$$

C_1 is the first coefficient in the Gegenbauer expansion, and z is the ratio of the quark momentum fraction to the longitudinal momentum transfer to the quark. Our starting points in the analysis are the global fits presented in refs [10,11], referred to as Kumerički–Müller parameterization. The imaginary part of the amplitude is calculated from a parameterization of the GPDs along the diagonal $x=\xi$. The real part of the amplitude is then reconstructed by assuming leading-order dominance and applying the dispersion relation. The ξ-dependence of the D-term is completely generated by the Gegenbauer expansion and restricted to the $d_1(t)$ term only. Finally, the momentum transfer dependence of the $d_1(t)$ term is given as a function of the three parameters $d_1(0)$, M and α:

$$d_1(t)=d_1(0)\left(1-\frac{t}{M^2}\right)^{-\alpha}$$

where M and α are parameters adjusted to the data, and the chosen form of $d_1(t)$ with $\alpha=3$ is consistent with the asymptotic behaviour required by the dimensional counting rules in QCD[20]. We adjust and fix the central values of the model parameters to DVCS data obtained at an electron beam energy of 6 GeV[21,22] which include unpolarized and polarized beam cross-sections over a wide phase space in the valence region and support the model that suggests that the GPD H largely dominates these observables. The fit to the beam-spin asymmetries is shown in Fig. 2, and that to the unpolarized cross-sections in Fig. 3. A fit to $d_1(t)$ is provided in Fig. 4; the data points correspond to the values extracted from the fit in Fig. 3. The analysis of the experimental results shows that $d_1(0)$ has a negative sign, consistent with several theoretical studies[16,23,24]. The fit results give $d_1(0)=-2.04$ with statistical uncertainty 0.14 and systematic uncertainty 0.33, where the uncertainties are

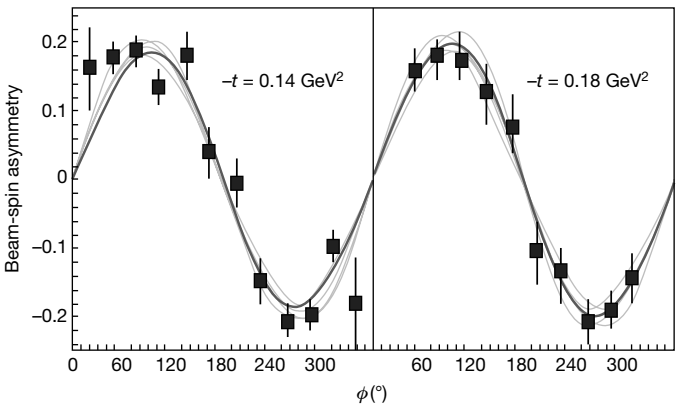

Fig. 2 | Fits to the beam-spin asymmetry results. The experimental results (squares) are shown as a function of the angle ϕ between the electron and recoil scattering planes. The sine-like behaviour of the data is due to the interference of DVCS and Bethe–Heitler processes. The fit is shown as the thick dark curve. The thin light-grey curves correspond to variations of the fitting parameters to the imaginary part of the CFF $\mathcal{H}$, as calculated from a Kumerički–Müller parameterization[10] adjusted to the data. Uncertainties represent one standard deviation.

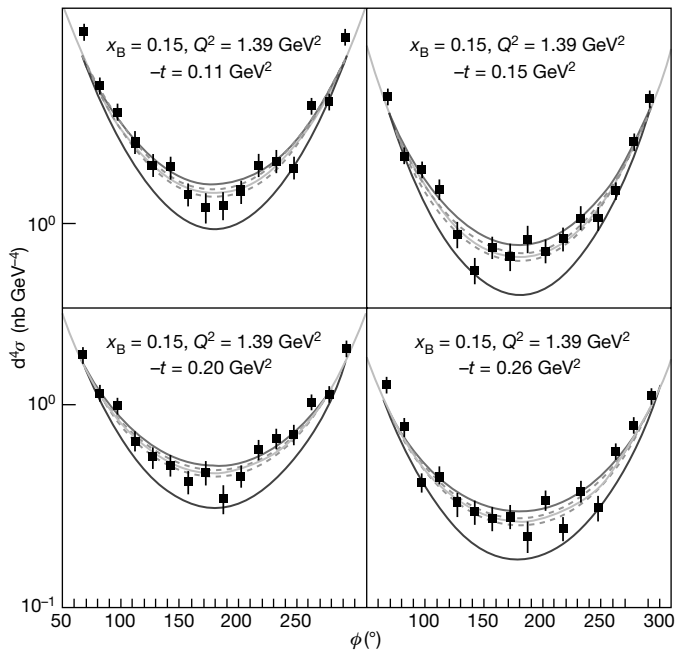

Fig. 3 | Examples of fits to unpolarized cross-sections. Experimental DVCS cross-sections[22] (black squares) are shown as a function of ϕ at fixed values of x_B and Q^2. Q^2 is the virtuality of the exchanged photon, and x_B is the momentum fraction of the struck quark. The light-grey curves show the results of the local fits with the parameter $d_1(t)$ at fixed $-t$, including one standard deviation. The upper, dark-grey curves are the results of global fits to the $-t$ dependence of $d_1(t)$, with the real part of the DVCS amplitude calculated from the dispersion relations and the subtraction term evaluated from the $d_1(t)$ contribution. The Bethe–Heitler contribution is shown with the lower, black curve. Its contribution to the cross-section dominates the extreme regions of ϕ. Uncertainties represent one standard deviation.

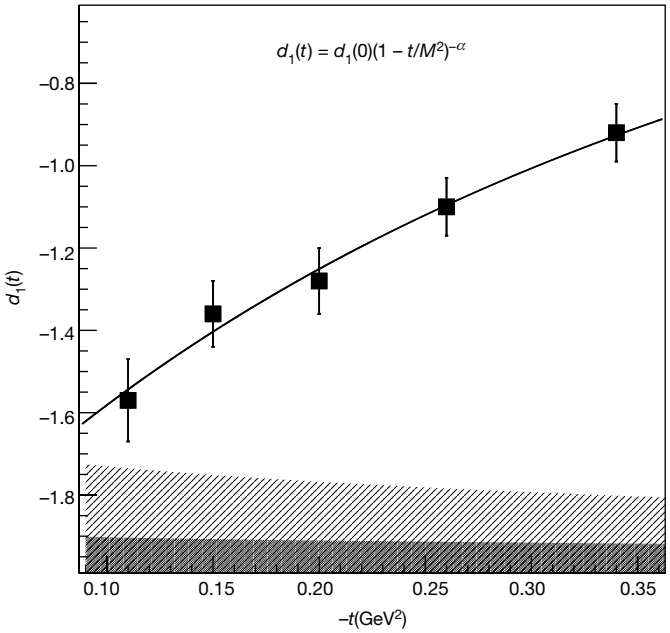

Fig. 4 | Example of a fit to gravitational form factor $d_1(t)$. The error bars are from the fit to the cross-sections at a fixed value of $-t$. The light-shaded area at the bottom corresponds to the uncertainties from the extension of the fit into regions without data and coincides with the light-green shaded area in Fig. 1. The dark-shaded area corresponds to the projected uncertainties for a future experiment[30] at 12 GeV, as shown by the red-shaded area in Fig. 1. Uncertainties represent one standard deviation.

given as one standard deviation. The negative sign of $d_1(0)$ found in this analysis seems deeply rooted in the spontaneous breakdown of chiral symmetry[25], which is a consequence of the transition of the micro-second-old Universe from a state of de-confined quarks and gluons to a state of confined quarks in stable protons. It is thus intimately connected with the stability of the proton[24] and of the visible Universe.

We can relate $d_1(t)$ to the pressure distribution via the spherical Bessel integral:

$$d_1(t) \propto \int \frac{j_0(r\sqrt{-t})}{2t} p(r)\mathrm{d}^3 r$$

where j_0 is the first spherical Bessel function. Our results of the quark pressure distribution in the proton are illustrated in Fig. 1. The thick black line corresponds to the pressure distribution $r^2p(r)$, as extracted from the D-term parameters that are fitted to the published data[22] acquired at 6 GeV. The estimated uncertainties are displayed as the light-green shaded area. The red-shaded area represents projected results from future experiments at higher energy. The distribution has a positive core and a negative tail of the $r^2p(r)$ distribution as a function of r, with a zero crossing near $r = 0.6$ fm. The regions where repulsive and binding pressures dominate are separated in radial space, with the repulsive distribution peaking near $r = 0.25$ fm, and the maximum of the negative pressure that is responsible for the binding occurring near $r = 0.8$ fm.

The outer, blue-shaded area in Fig. 1 corresponds to the D-term uncertainties obtained in the global fit results from previous research[10,11]. This area has a shape similar to the light-green area, confirming the robustness of the analysis procedure used to extract the D-term. The pressure $p(r)$ must satisfy the stability condition:

$$\int_0^\infty r^2 p(r)\mathrm{d}r = 0$$

which is satisfied within the uncertainties of our analysis. The shape of the radial pressure distribution resembles closely that obtained using the chiral quark–soliton model[24], in which the proton is modelled as a chiral soliton whose constituent quarks are bound by a self-consistent pion field. This agreement suggests that the pion field is appropriate for the description of the proton as a bound state of quarks.

Other applications of the GFFs of the energy–momentum tensor include the description of nucleons in the nuclear medium[23,26,27], excited baryon states (such as the $\Delta(1232)$ resonance[28]) and point-like and composed spin-0 particles[29].

Future precision experiments are expected to provide substantially more DVCS data[30] and enable the mapping of $d_1(t)$ in much finer steps and in a much larger $-t$ range, which will reduce the systematic uncertainties, as indicated by the red-shaded area in Fig. 1. We also expect that this work will motivate new theoretical efforts to understand the fundamental characteristics of the stability of the proton from first principles. Our results may serve as a benchmark for the assessment of theoretical models, including lattice quantum chromodynamics models.

Online content

Any Methods, including any statements of data availability and Nature Research reporting summaries, along with any additional references and Source Data files, are available in the online version of the paper at https://doi.org/10.1038/s41586-018-0060-z.

Received: 25 August 2017; Accepted: 16 February 2018;
Published online 16 May 2018.

1. Ji, X. D. Deeply virtual Compton scattering. *Phys. Rev. D* **55**, 7114–7125 (1997).
2. Ji, X. D. Gauge-invariant decomposition of nucleon spin. *Phys. Rev. Lett.* **78**, 610–613 (1997).
3. Ozel, F. & Freire, P. Masses, radii, and equation of state of neutron stars. *Annu. Rev. Astron. Astrophys.* **54**, 401–440 (2016).
4. Pagels, H. Energy–momentum structure form factors of particles. *Phys. Rev.* **144**, 1250–1260 (1966).
5. Teryaev, O. V. Gravitational form factors and nucleon spin structure. *Front. Phys.* **11**, 111207 (2016).
6. Belitsky, A. V. & Radyushkin, A. V. Unraveling hadron structure with generalized parton distributions. *Phys. Rep.* **418**, 1–387 (2005).
7. Müller, D., Robaschik, D., Geyer, D., Dittes, F. M. & Horejši, J. Wave functions, evolution equations and evolution kernels from light-ray operators of QCD. *Fortschr. Phys.* **42**, 101–141 (1994).
8. Radyushkin, A. V. Scaling limit of deeply virtual Compton scattering. *Phys. Lett. B* **380**, 417–425 (1996).
9. Polyakov, M. V. Generalized parton distributions and strong forces inside nucleons and nuclei. *Phys. Lett. B* **555**, 57–62 (2003).
10. Kumerički, K. & Müller, D. Deeply virtual Compton scattering at small x_B and the access to the GPD H. *Nucl. Phys. B* **841**, 1–58 (2010).
11. Müller, D., Lautenschlager, T., Passek-Kumericki, K. & Schaefer, A. Towards a fitting procedure to deeply virtual meson production – the next-to-leading order case. *Nucl. Phys. B* **884**, 438–546 (2014).
12. Guidal, M., Moutarde, H. & Vanderhaeghen, M. Generalized parton distributions in the valence region from deeply virtual Compton scattering. *Rep. Prog. Phys.* **76**, 066202 (2013).
13. Kumerički, K., Liuti, S. & Moutarde, H. GPD phenomenology and DVCS fitting: entering the high-precision era. *Eur. Phys. J. A* **52**, 157 (2016).
14. Diehl, M. & Ivanov, D. Y. Dispersion representations for hard exclusive processes: beyond the Born approximation. *Eur. Phys. J. C* **52**, 919–932 (2007).
15. Anikin, I. V. & Teryaev, O. V. Dispersion relations and QCD factorization in hard reactions. *Fizika B* **17**, 151–158 (2008).
16. Pasquini, B., Polyakov, M. V. & Vanderhaeghen, M. Dispersive evaluation of the D-term form factor in deeply virtual Compton scattering. *Phys. Lett. B* **739**, 133–138 (2014).
17. Polyakov, M. V. & Weiss, C. Skewed and double distributions in the pion and the nucleon. *Phys. Rev. D* **60**, 114017 (1999).
18. Radyushkin, A. V. Modeling nucleon generalized parton distributions. *Phys. Rev. D* **87**, 096017 (2013).
19. Radyushkin, A. V. Sum rules for nucleon generalized parton distributions and border function formulation. *Phys. Rev. D* **88**, 056010 (2013).
20. Lepage, G. P. & Brodsky, S. J. Exclusive processes in perturbative quantum chromodynamics. *Phys. Rev. D* **22**, 2157–2198 (1980).
21. CLAS Collaboration. Measurement of deeply virtual Compton scattering beam-spin asymmetries. *Phys. Rev. Lett.* **100**, 162002 (2008).
22. CLAS Collaboration. Cross sections for the exclusive photon electroproduction on the proton and generalized parton distributions. *Phys. Rev. Lett.* **115**, 212003 (2015).
23. Kim, H. C., Schweitzer, P. & Yakhshiev, U. Energy–momentum tensor form factors of the nucleon in nuclear matter. *Phys. Lett. B* **718**, 625–631 (2012).
24. Goeke, K. et al. Nucleon form factors of the energy–momentum tensor in the chiral quark–soliton model. *Phys. Rev. D* **75**, 094021 (2007).

25. Kivel, N., Polyakov, M. V. & Vanderhaeghen, M. Deeply virtual Compton scattering on the nucleon: study of the twist-3 effects. *Phys. Rev. D* **63**, 114014 (2001).
26. Eides, M. I., Petrov, V. Y. & Polyakov, M. V. Narrow nucleon–ψ(2S) bound state and LHCb pentaquarks. *Phys. Rev. D* **93**, 054039 (2016).
27. Jung, J. H., Yakhshiev, U., Kim, H. C. & Schweitzer, P. In-medium modified energy–momentum tensor form factors of the nucleon within the framework of a π–ρ–ω soliton model. *Phys. Rev. D* **89**, 114021 (2014).
28. Perevalova, I. A., Polyakov, M. V. & Schweitzer, P. LHCb pentaquarks as a baryon–ψ(2S) bound state: prediction of isospin-3/2 pentaquarks with hidden charm. *Phys. Rev. D* **94**, 054024 (2016).
29. Hudson, J. & Schweitzer, P. *D* term and the structure of pointlike and composed spin-0 particles. *Phys. Rev. D* **96**, 114013 (2017).
30. CLAS Collaboration *Deeply Virtual Compton Scattering with CLAS12 at 6.6 GeV and 8.8 GeV*. Proposal E12–16–010B (Jefferson Lab PAC44, 2016); https://www.jlab.org/exp_prog/proposals/16/PR12-16-010B.pdf.

Acknowledgements We thank M. Polyakov and P. Schweitzer for discussions on the subject matter of this work. We are indebted to G. D. Cates for reading the manuscript and suggesting text improvements. This material is based on work supported by the US Department of Energy, Office of Science, Office of Nuclear Physics under contract DE-AC05-06OR23177.

Reviewer information Nature thanks G. D. Cates and the other anonymous reviewer(s) for their contribution to the peer review of this work.

Author contributions V.D.B. wrote the manuscript initiated the analysis, and coordinated and oversaw the research and the validation of the results. L.E. worked with theory experts on the feasibility of the present analysis to develop a procedure connecting the data to the pressure measurements and worked on the analysis of the DVCS beam spin asymmetry. F.X.G. provided the detailed analysis of beam asymmetry and the cross-section measurements, performed the fits to extract the D-term and used the dispersion relation analysis to relate the results to the confinement form factor $d_1(t)$.

Competing interests The authors declare no competing interests.

Additional information
Extended data is available for this paper at https://doi.org/10.1038/s41586-018-0060-z.
Reprints and permissions information is available at http://www.nature.com/reprints.
Correspondence and requests for materials should be addressed to V.D.B.
Publisher's note: Springer Nature remains neutral with regard to jurisdictional claims in published maps and institutional affiliations.

METHODS

Here we provide additional details about the method of extraction of the CFFs using dispersion relations, from which the D-term and $d_1(t)$ are computed. In the first step, the beam-spin asymmetries and unpolarized cross-sections are fitted simultaneously, and the CFFs are obtained locally as the real and imaginary parts of the amplitude at one particular kinematical point. In the second step, the CFFs are fitted globally with the Kumerički–Müller parameterization[10,11], the real part of the amplitude is calculated by the dispersion integral from the imaginary part of the amplitude, and the D-term is derived as a subtraction, as described in the text.

To illustrate the robustness of our results, in Extended Data Fig. 1 we show the locally extracted CFFs Im$\mathcal{H}$ and Re$\mathcal{H}$ separately as a function of ξ, for a fixed t value. These locally extracted amplitudes (black squares) are compared to the global parameterization (central red curve, with the grey bands showing the estimated uncertainties). The left panel shows the imaginary part of the amplitude $\mathcal{H}$, which is mostly sensitive to beam-spin asymmetries, together with the amplitude parameterization as a function of ξ at $-t = 0.13\,\mathrm{GeV}^2$. The interpretation of the error bands as separate contributions from different uncertainties in the parameterization, after adjustment to our data, are discussed in more detail below. The right panel shows the real part of the amplitude, which is mostly sensitive to the unpolarized cross-sections. The different numbers of points in the polarized and unpolarized cross-sections come from the real and imaginary parts of the amplitude being sensitive to different ranges in the azimuthal angle ϕ. The real part of the amplitude is more sensitive in the central range around $\phi = 180°$, where the statistics and the acceptances are reduced—as a consequence, Re$\mathcal{H}$ cannot be determined when ξ increases.

The central red curve in each panel is the result of our global fit. The grey band between the thick red lines shows the uncertainties of the contribution from the other CFFs, on which our data do not provide strong constraints. The red band shows the total error of the global fit to the imaginary part of the amplitude, including fitting errors of the model parameters, in addition to the above uncertainties. In our framework, these grey and red bands are propagated through the dispersion integral as direct uncertainties in the real part of the amplitude. The additional blue band in the right panel illustrates the total error of the real part of the amplitude, including that of the extracted D-term. We note that the uncertainties in the D-term increase with $-t$, as reflected by the larger uncertainties in the spatial distribution at short distances, even after r^2 weighting.

For completeness, we show in Extended Data Fig. 2 and Extended Data Fig. 3 the real and imaginary parts of the amplitude for the other four $-t$ values that are shown in Fig. 4 as a function of ξ. Our data show a behaviour similar to the Kumerički–Müller parameterization at the lower $-t$ value, but begin to depart from the calculations at higher $-t$ values. The assumption $D(t) = 0$, shown by the black line, is inconsistent with our full results. This confirms that finite values of $D(t)$ are required and again demonstrates the robustness of our results shown in Fig. 1.

Data availability. The data used in this work are publicly available at http://clasweb.jlab.org/physicsdb/intro.html.

Code availability. The code used in the data analysis is available at https://userweb.jlab.org/~fxgirod/code_paperFeb18. The data reduction program uses the standard C++ ROOT framework, which was developed at CERN and is freely available under a GNU Lesser General Public License at https://root.cern.ch. The source code to reproduce the figures is freely available at https://userweb.jlab.org/~fxgirod/code_paperFeb18/.

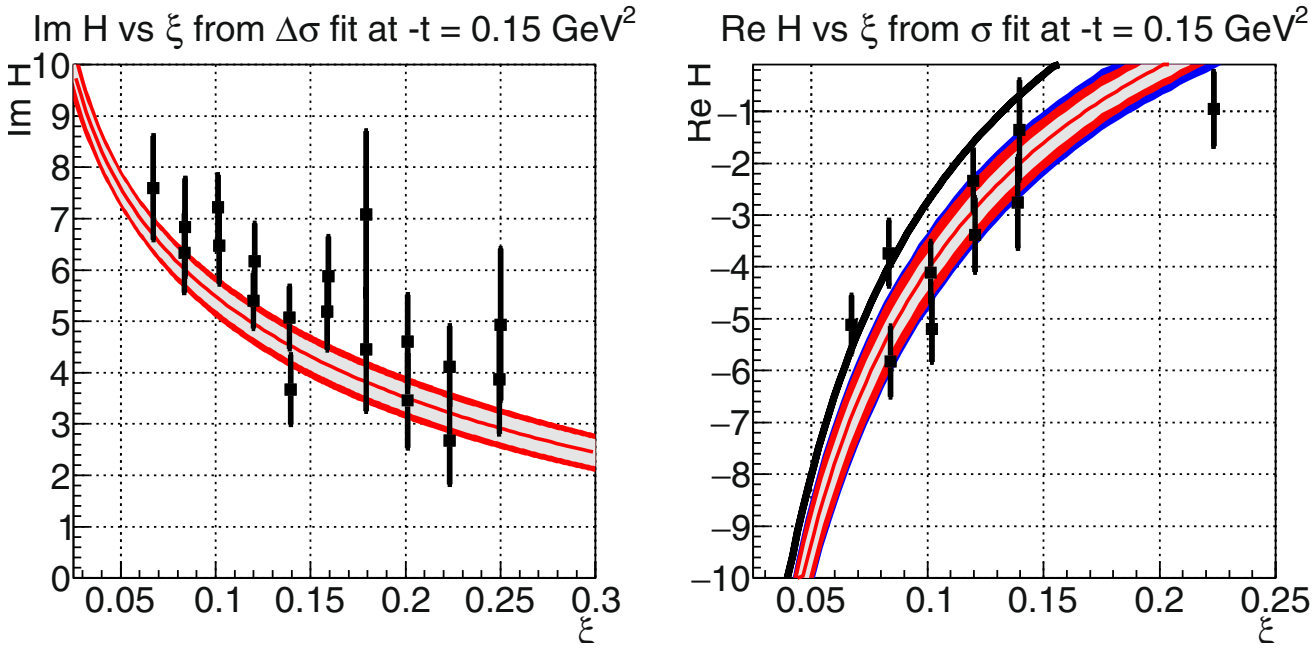

Extended Data Fig. 1 | Compton form factor $\mathcal{H}$ at $-t = 0.15\,\mathrm{GeV}^2$. The graphs show the imaginary (left) and real (right) parts of $\mathcal{H}$ versus the momentum transfer to the quark, ξ. The inner red curve shows the result of our global fit. The grey band shows the estimated uncertainties from the contributions of other CFFs, the outer red band shows the total uncertainties of the imaginary part of the amplitude, and the outer blue band (right) includes the uncertainties related to the D-term. All uncertainties represent one standard deviation.

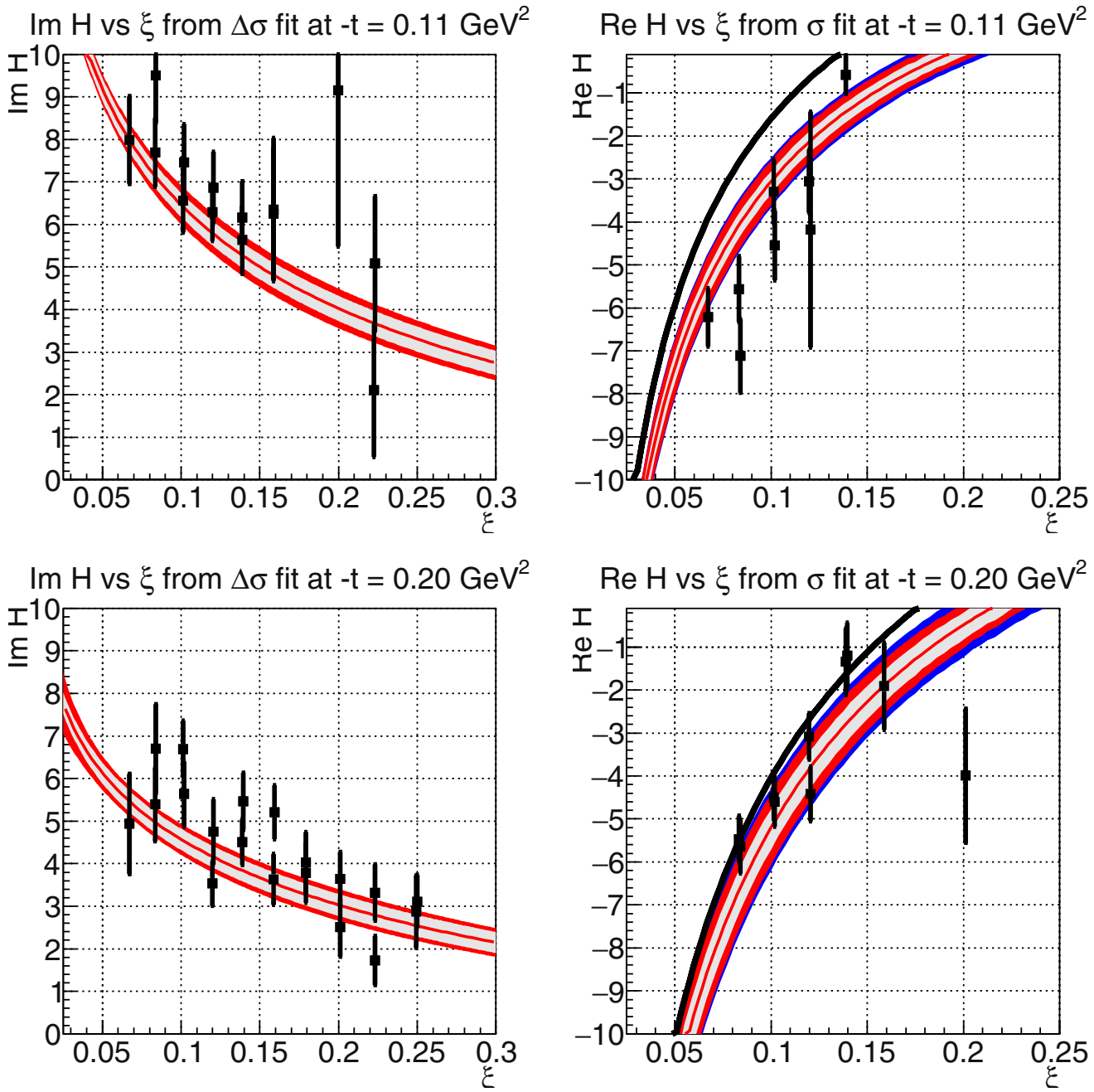

Extended Data Fig. 2 | Compton form factor $\mathcal{H}$ at $-t = 0.11\,\mathrm{GeV}^2$ and at $-t = 0.20\,\mathrm{GeV}^2$. The imaginary (left) and real (right) parts of $\mathcal{H}$ are shown as a function of ξ. The red curve and the grey, red and blue bands are as in Extended Data Fig. 1. All uncertainties represent one standard deviation.

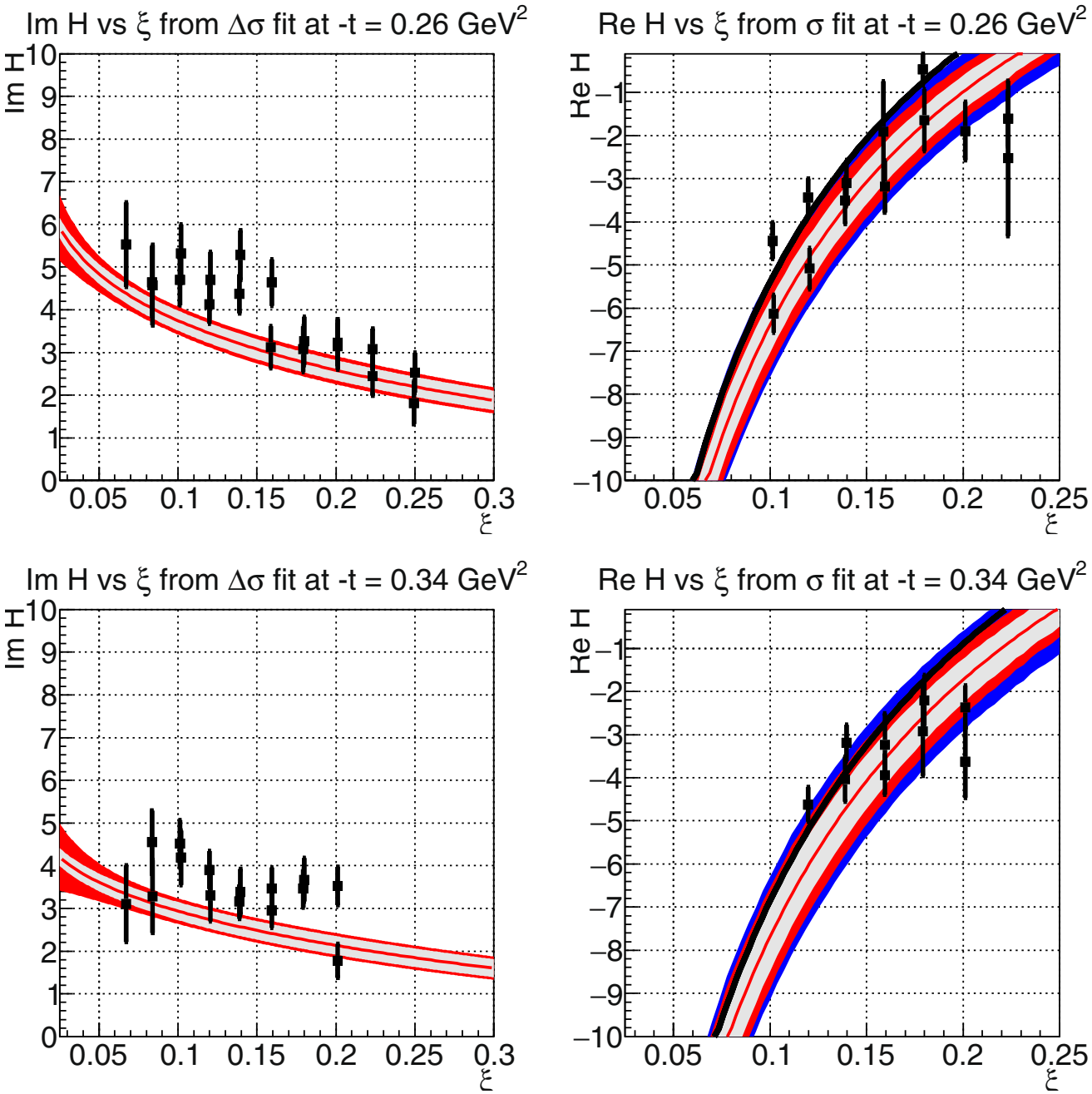

Extended Data Fig. 3 | Compton form factor $\mathcal{H}$ at $-t = 0.26\,\mathrm{GeV}^2$ and at $-t = 0.34\,\mathrm{GeV}^2$. The imaginary (left) and real (right) parts of $\mathcal{H}$ are shown as a function of ξ. The red curve and the grey, red and blue bands are as in Extended Data Fig. 1. All uncertainties represent one standard deviation.